Journal of Science and Technology – Smart Systems and Devices
Volume xx, Issue x, Month 2026, ppp–ppp

An IoT-Based Heart Rate and SpO_2 Wearable Device for Centralized Patient Monitoring in Viet Nam: Design and Preliminary Assessment

Dung Nguyen Hoang*
Hanoi University of Science and Technology, Ha Noi, Vietnam
**Corresponding author email: dung.nguyenhoang@hust.edu.vn*

Abstract

This paper presents the design and experimental prototyping of a wristwatch-style smart wearable device based on Internet of Thing (IoT) architecture for continuous centralized monitoring of heart rate and blood oxygen saturation (SpO_2). To address the critical limitations of prior works that remain constrained to isolated, individual-scale trials, the proposed solution establishes an optimized network topology that enables a centralized server to concurrently and synchronously manage high-throughput data streams from multiple distributed nodes. The hardware architecture optimizes microcircuit real estate on a 2-layer printed circuit board (PCB) platform with a compact dimension of 40 x 30 mm, integrating a high-performance dual-core ESP32-S3 microcontroller, a MAX30102 optical biosensing module, a DS3231 real-time clock (RTC), and an ST7789 TFT display interface. To effectively eliminate wrist-specific motion artifacts, an on-chip Adaptive Edge-based Kalman Filter (AE-KF) algorithm is implemented directly to preserve the underlying physiological morphology of the photoplethysmography (PPG) waveforms. The preprocessed time-series data are encapsulated into a JSON payload structure and transmitted in real-time to a centralized dashboard via the lightweight Message Queuing Telemetry Transport (MQTT) protocol over a Wi-Fi wireless network. The system was experimentally evaluated on a sample cohort of 100 elderly volunteers (aged 50 to 80 years) under both sedentary resting states and light physical activities, cross-referenced directly against a clinically validated LK87 fingertip pulse oximeter as the baseline gold standard. The empirical results confirm the superior accuracy of the proposed system: the root-mean-square error (RMSE) for heart rate monitoring is 1.5229 bpm with a strict Bland-Altman limit of agreement within ±3 bpm, and the SpO_2 measurement RMSE remains stable below 0.65. This study establishes a standardized data infrastructure ready for advanced machine learning algorithms to enable early clinical risk prognosis and remote preventive healthcare.

Keywords: ESP32-S3, heat rate, IoT, PPG, SpO_2.

1. Introduction

The global paradigm shift in healthcare from a centralized, hospital-centric model toward proactive and decentralized care has engendered an imperative demand for Remote Patient Monitoring (RPM) systems. Concurrently, rapid advancements in sensor technologies, embedded systems, wireless communications, and artificial intelligence (AI) have propelled smart wearables into a highly promising research avenue within the health monitoring domain. Wearable systems facilitate continuous, non-invasive physiological data acquisition while optimizing user convenience relative to traditional clinical modalities. Among primary vital signs, heart rate and blood oxygen saturation (SpO_2) constitute core indicators for rapid evaluation of the cardiovascular and respiratory systems, as well as for the early detection of pathological anomalies. Recent literature reviews further establish that the wristband or smartwatch form factor represents the most prevalent and optimal design configuration for remote healthcare architectures [1].

In tandem with hardware advancements, the convergence of the Internet of Things (IoT) and Artificial Intelligence (AI)–collectively termed the AIoT architecture–paves the way for highly connected and scalable health monitoring systems. Within this paradigm, wearable devices function as edge nodes for data acquisition, subsequently transmitting information to a centralized server for real-time storage, management, and analytics. However, the vast majority of existing literature remains constrained to individual-scale trials or isolated prototype designs. The capacity for concurrent multi-device connectivity and synchronized multi-user data aggregation on a centralized server platform remains a critical, unresolved technical challenge. Overcoming this technological limitation is imperative, particularly as hospitals, clinics, and telehealth frameworks demand the capacity to continuously and simultaneously monitor a massive volume of patients [2].

To address these challenges, this paper proposes the design and development of an IoT-oriented medical wearable device aimed at the continuous wrist-based monitoring of heart rate and SpO_2 levels. The hardware architecture optimizes microcircuit real estate by integrating a biosensing module, a central processing unit, power management circuitry, and a low-power wireless communication interface, thereby ensuring an

p-ISSN 3093-3285
e-ISSN 3093-3315
https://doi.org/10.51316/jst.xxx.ssad.2026.xx.x.x
Received: May 22, 2026; Revised: Jun 4, 2026;
Accepted: Jun 16, 2026; Online: Jun 30, 2026

efficient pipeline for data acquisition, edge processing, and real-time transmission. The scientific contribution of this study is manifested in its network topology, which enables a centralized server to concurrently manage distributed data from multiple wearable nodes, thus optimizing wide-area patient monitoring workflows for healthcare facilities. Furthermore, this synchronized system establishes a standardized data infrastructure, paving the way for the integration of machine learning algorithms to analyze vital sign trends, forecast clinical risks, and advance the digital telehealth ecosystem.

2. Theoretical Background

2.1. Photoplethysmographic Principles

Photoplethysmography (PPG) is a non-invasive optical measurement technique utilized to detect volumetric variations of blood within the microvasculature of biological tissue. The underlying operational principle relies on emitting optical radiation into the tissue via a light-emitting diode (LED) and subsequently quantifying the light intensity captured by a photodetector following absorption, scattering, and reflection within the intra-tissue matrix. As arterial blood volume fluctuates cyclically in accordance with the cardiac cycle, the optical absorption characteristics of the bulk tissue undergo corresponding variations. Consequently, the output light intensity is modulated over time, yielding the characteristic PPG waveform. Owing to its non-invasive nature, minimalist hardware footprint, and high integration capability, PPG has emerged as a foundational modality for contemporary optical-based physiological monitoring architectures [3, 4]. The attenuation of light intensity traveling through biological tissue structures is described by the Modified Beer–Lambert Law, expressed as follows:

$$I = I_0 \mathrm{e}^{-\mu effL} \tag{1}$$

where I_0 signifies the incident light intensity from the light source, I is the optical intensity captured at the photodetector, μeff is the effective optical attenuation coefficient of the medium, and L represents the actual optical path length within the tissue matrix.

From (1), the optical absorbance A is mathematically expressed as:

$$A = \ln\left(\frac{I_0}{I}\right) = \mu effL \tag{2}$$

The mathematical expressions demonstrate that changes in the optical density of the medium - specifically the time-varying fluctuations in arterial blood volume - consequently dictate the amplitude variations of the optical signal captured by the sensor. Fig. 1 illustrates the cardiac-synchronous alternating current (AC) component of the PPG signal alongside the corresponding electrocardiogram (ECG) waveform. From a signal dynamics perspective, the empirical PPG signal is decomposed into two primary components: a slowly varying direct current (DC) baseline and an alternating current (AC) component that oscillates synchronously with the cardiac cycle. Accounting for external noise sources and peripheral artifacts, the generalized mathematical model of the PPG signal is formulated as follows:

$$s_{\mathrm{PPG}}(t) = \mathrm{DC}(t) + \mathrm{AC}(t) + n(t) \tag{3}$$

where DC(t) accounts for the baseline optical absorption of stationary tissue matrices, venous blood, and low-frequency fluctuations derived from respiration and vasomotor regulation; AC(t) denotes the pulsatile arterial blood volume variations synchronized with individual myocardial contractions; and $n(t)$ encapsulates the random noise and motion artifacts encountered during data acquisition [3, 5].

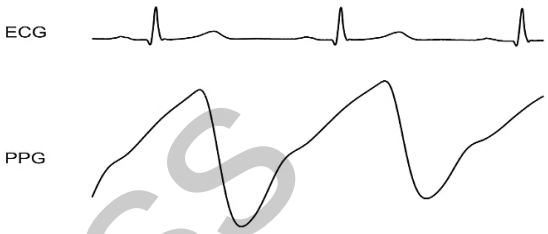

Fig. 1. The pulsatile alternating current (AC) component of the PPG signal and the corresponding electrocardiogram (ECG) signal

The alternating current (AC) component of the PPG signal exhibits a direct linear relationship with arterial blood volume variations, which is modeled according to the following expression:

$$\mathrm{AC}(t) = \alpha \Delta V_{\mathrm{art}}(t) \tag{4}$$

where $\Delta \mathrm{V}_{art}(\mathrm{t})$ signifies the time-dependent variation of arterial blood volume, and α is a proportionality coefficient governed by the light wavelength and the optical characteristics of the tissue matrix. Consequently, the amplitude and waveform of the PPG signal enable the extraction of hemodynamic information from the circulatory system, serving as the mathematical foundation to determine heart rate and develop blood oxygen saturation (SpO_2) estimation algorithms in the subsequent sections [3, 4].

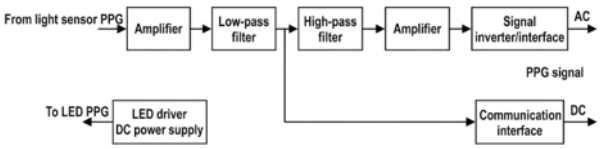

Fig. 2. Block diagram of the signal conditioning circuitry in the PPG measurement

To effectively extract physiological features from the optical sensor, the raw signal must be processed through signal conditioning stages prior to feature extraction. The overall block diagram of the PPG signal conditioning system is illustrated in Fig. 2, comprising the following primary functional blocks: (1) Transimpedance Amplifier (TIA) stage: Converts the

photocurrent from the photodiode into a proportional voltage signal; (2) Active filters (High-Pass Filter - HPF and Low-Pass Filter - LPF): The HPF suppresses the DC offset to isolate the cardiac-synchronous AC component, while the LPF (typically configured with a cutoff frequency < 10 Hz) eliminates white noise and high-frequency interference; (3) Gain stage: Optimizes the signal amplitude to precisely decouple and quantify the AC and DC constituents of the PPG signal [1] for subsequent heart rate calculation and blood oxygen saturation (SpO_2) estimation. Consequently, the PPG method not only provides a clear representation of cardiovascular periodicity but also establishes the core physical foundation for deriving vital physiological parameters, including heart rate, blood oxygen saturation (SpO_2), and advanced hemodynamic characteristics. For wrist-worn wearable devices, this approach offers substantial practical utility owing to its capacity for continuous, non-invasive data acquisition, thereby rigorously satisfying the stringent requirements of real-time health surveillance.

2.2. Methodology for Heart Rate Determination from PPG Signal

The heart rate is determined by exploiting the periodicity of the alternating current component, AC(t), within the PPG signal, which represents the arterial blood volume fluctuations driven by the myocardial contraction cycle. Under standard physiological conditions, each cardiac cycle generates a characteristic time-domain PPG pulse. Consequently, the heart rate estimation task fundamentally resolves into identifying periodic temporal landmarks across the PPG pulse train. For contemporary wrist-worn wearable platforms, two prominent paradigms are widely adopted: (1) *Time- domain analysis*, which computes the heart rate via the temporal intervals between consecutive characteristic features (e.g., peak-to-peak intervals), and (2) *Frequency-domain analysis*, which identifies the heart rate by extracting the dominant frequency utilizing spectral transformation algorithms. Recent literature reviews validate these two approaches as foundational frameworks for PPG-based heart rate monitoring, which are particularly optimized for the hardware architectures of wearable devices [5].

2.2.1. Time-domain analysis methods for heart rate estimation

Let t_i denote the occurrence time (or timestamp) of the characteristic landmark (such as the systolic peak) at the i-th cardiac cycle. The time interval between two consecutive beats, or the Inter-Beat Interval (IBI), is determined by the temporal difference between two successive landmarks:

$$\mathrm{IBI}_{(i)} = t_{i+1} - t_i \tag{5}$$

where the variable $\mathrm{IBI}_{(i)}$ is measured in seconds (s). From this quantity, the instantaneous heart rate $\mathrm{HR}_{\mathrm{inst}\,(i)}$, in beats per minute - bpm, is determined by the expression:

$$\mathrm{HR}_{\mathrm{inst}\,(i)} = \frac{60}{\mathrm{IBI}_{(i)}} \tag{6}$$

To mitigate short-term fluctuations and limit localized errors induced by noise, the average heart rate (HR_{avg}) within an observation window comprising N consecutive cycles is structured according to the arithmetic mean model:

$$\mathrm{HR}_{avg} = \frac{1}{N}\sum_{i=1}^{N} \mathrm{HR}_{\mathrm{inst}\,(i)} \tag{7}$$

This time-domain mathematical approach is particularly well-suited for real-time embedded systems owing to its low computational complexity, minimal memory footprint, and straightforward implementation on low-power microcontrollers.

2.2.2. Frequency-domain analysis methods for heart rate estimation

In addition to the time-domain approach, the heart rate parameter can also be extracted in the frequency domain by identifying the peak spectral frequency (dominant frequency), f_{peak}, of the PPG signal following bandpass filtering and amplitude normalization. The generalized heart rate value is established based on a linear relationship with this spectral frequency:

$$\mathrm{HR} = f_{peak} \times 60 \tag{8}$$

where f_{peak} denotes the peak spectral frequency measured in Hertz (Hz). This spectral analysis method demonstrates high efficacy in scenarios where the PPG waveform morphology undergoes localized amplitude distortion, yet the overall periodicity of the signal remains preserved. However, under vigorous physical activity conditions, motion artifacts tend to generate high-energy spurious spectral peaks. These parasitic peaks directly compete with the actual heart rate frequency, thereby degrading the reliability of conventional peak-tracking algorithms. For this reason, software architecture in modern wearable devices often simultaneously integrate both time-domain and frequency-domain algorithms to optimize the robustness of the measurement.

2.2.3. Engineering challenges and preprocessing methodologies in wrist-based sensing

For wrist-worn wearable devices, the primary technical hurdle compromising algorithmic accuracy is motion artifacts (MAs). This factor severely distorts the waveform morphology of the pulse, obliterating true peaks, inducing spurious peaks, or displacing characteristic temporal landmarks, thereby leading to progressive errors in computing the corresponding interbeat interval (IBI) and heart rate values [6, 7]. In addition to motion artifacts, the quality of PPG signals acquired at the wrist is directly influenced by peripheral dynamic and physiological factors, including: (1) the physical contact location of the optical sensor; (2) the

mechanical pressure (tightness) of the strap; (3) the optical absorption and scattering characteristics of the skin and soft tissues; (4) the peripheral perfusion index (PI); and (5) optical interference from ambient light.

2.2.4. Adaptive edge-based kalman filter for PPG denoising

The core architecture of the proposed Adaptive Edge-based Kalman Filter (AE-KF) relies on a dynamic state-space formulation designed to track the rapid morphological transitions of the PPG waveform. The discrete state-update equation is formulated as:

$$x_k = Ax_{k-1} + w_k \tag{9}$$

where x_k represents the estimated clean PPG amplitude alongside its first derivative, and $w_k \sim N(0, Q_k)$ denotes the process noise. To prevent over-smoothing of critical systolic peaks during intensive physical activities, the time-varying covariance matrix Q_k is adaptively scaled by a localized edge-detection operator. This operator calculates the directional derivative of the input signal stream over a sliding temporal window. Upon detecting an abrupt gradient deviation indicative of a motion artifact, the measurement noise covariance R_k is instantly inflated relative to Q_k, forcing the filter to place higher reliance on the state prediction model rather than the corrupted measurement vector

$$z_k = Hx_k + v_k \tag{10}$$

this adaptive edge-bound tuning ensures robust baseline tracking and superior artifact suppression while preserving the underlying physiological morphology.

In our research, x_k denote the true PPG amplitude to be estimated at time step k. The noisy measurement acquired from the ADC of the MAX30102 sensor is represented by z_k; w_k and v_k correspond to the process noise and measurement noise, respectively. These covariance parameters are dynamically configured on the ESP32-S3 microcontroller to suppress micro-oscillations induced by subtle wrist movements.

2.3. Dual-Wavelength Methodology for SpO_2 Estimation from PPG Signals

Peripheral oxygen saturation (SpO_2) is determined based on the variations in the optical absorption characteristics of oxyhemoglobin (HbO_2) and deoxyhemoglobin (Hb) at two distinct wavelengths. In pulse oximetry, the widely adopted wavelength pair comprises red light (approximately 660 nm) and near-infrared light (approximately 940 nm). Within these spectral regions, Hb exhibits a higher absorption coefficient in the red band, whereas HbO_2 absorbs more dominantly in the infrared band. This distinct optical behavior allows for the differentiation and quantification of the two hemoglobin oxygenation states through the acquired spectrophotometric signals [8].

At each wavelength, the acquired PPG signal consists of two primary components: the alternating current (AC) component, which reflects the arterial blood volume variations synchronized with the cardiac cycle, and the direct current (DC) component, representing the baseline optical absorption of the surrounding tissue, venous blood, and non-pulsatile blood fraction. On this basis, the intermediate metric utilized for SpO_2 estimation is the Ratio-of-Ratios (denoted as R), which is formulated as follows:

$$R = \frac{\mathrm{AC_{red}}/\mathrm{DC_{red}}}{\mathrm{AC_{IR}}/\mathrm{DC_{IR}}} \tag{11}$$

where $\mathrm{AC_{red}}$ and $\mathrm{DC_{red}}$ are the components correspond to the red wavelength, while $\mathrm{AC_{IR}}$ and $\mathrm{DC_{IR}}$ represent the components corresponding to the infrared wavelength. From the quantity R, the SpO_2 value is derived via an empirical calibration function, which is commonly linearly approximated as follows:

$$SpO_2 = A - BR \tag{12}$$

where A and B are calibration constants dependent on the geometric configuration of the sensor, the optical characteristics of the measurement system, and the empirical model of the device. Fig. 3 illustrates the absorption spectra of oxyhemoglobin and deoxyhemoglobin, demonstrating the rationale for selecting the red and infrared wavelengths in SpO_2 measurement. Inherently, the relationship between the R-value and peripheral oxygen saturation (SpO_2) cannot be absolutely determined solely by simplified theoretical absorption models, such as the Beer-Lambert law. This limitation arises because optical signals propagating through biological tissues are complexly influenced by light scattering phenomena, variations in the effective optical pathlength, and the intrinsic photobiological characteristics of the tissue. Consequently, practical pulse oximeters must establish calibration curves derived from controlled human desaturation studies, cross-referenced against the reference arterial oxygen saturation (SaO_2) measured via a co-oximeter. This necessity underscores why the SpO_2 estimation process is inextricably linked to empirical calibration phases rather than direct computation from purely theoretical formulations [9].

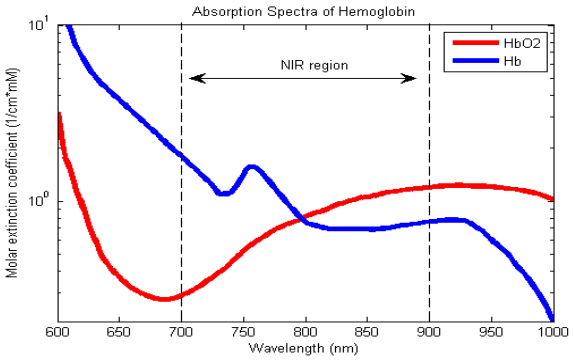

Fig. 3. Absorption spectra of oxyhemoglobin and deoxyhemoglobin, demonstrating the rationale for selecting red and infrared wavelengths in SpO_2 measurement

For wearable devices, particularly when deploying a reflectance configuration, the accuracy of SpO_2 measurement heavily depends on the efficiency of separating the alternating current (AC) and direct current (DC) components at both wavelengths. Real-world factors such as motion artifacts, variations in contact pressure at the sensor-skin interface, inter-individual differences in physiological morphology, and ambient measurement conditions can severely distort the *R*-ratio, directly impacting the error margin of the estimated SpO_2. Therefore, in practical deployment architectures, the SpO_2 computation workflow necessitates the integration of data preprocessing algorithms, Signal Quality Assessment (SQA) frameworks, and adaptive calibration models tailored to the specific hardware configuration [10].

3. System Design and Implementation

3.1. Hardware Design

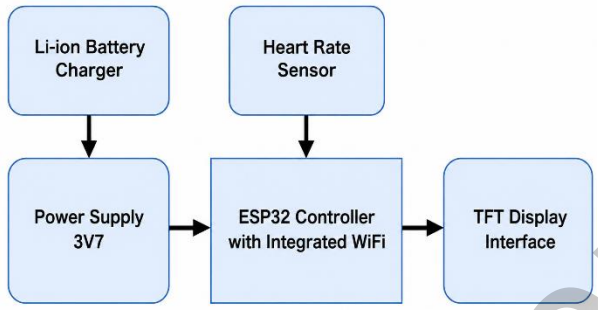

Fig. 4. Hardware block diagram of the wrist-worn heart rate and SpO_2 monitoring device

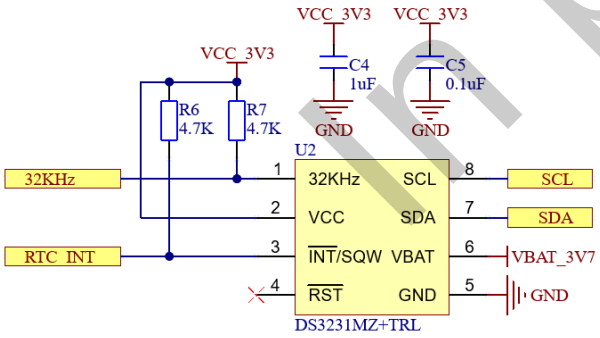

Fig. 5. Schematic diagram of the heart rate and SpO_2 sensor block utilizing the MAX30102

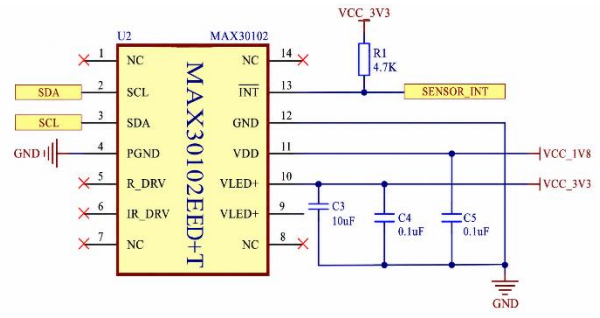

Fig. 6. Schematic diagram of the RTC DS3231

In this paper, the system is designed based on an integrated embedded architecture, where the ESP32-S3 microcontroller serves as the central processing unit (MCU) responsible for orchestrating all peripheral modules. The hardware architecture illustrated in Fig. 4 comprises four primary functional subsystems: a power management subsystem (utilizing an integrated **3.7 V** Li-ion battery and a charge management circuit), an optical biosensing subsystem (for heart rate and SpO_2 measurement), a real-time clock (RTC) module, a TFT display subsystem, and a wireless communication subsystem. Specifically, the PPG signal is captured by the dedicated MAX30102 sensor, then digitized and transmitted to the MCU via the I^2C protocol to execute preprocessing algorithms, physiological parameter extraction, and real-time data synchronization. In parallel, the TFT display connected via the Serial Peripheral Interface (SPI) provides local visualization of the measured metrics, while the on-chip integrated Wi-Fi module handles data transmission to the centralized monitoring platform. This architectural layout not only guarantees the operational autonomy and independence of the sensor node but also optimizes scalability for seamless integration into medical IoT ecosystems for multi-patient monitoring.

From a design perspective, the hardware architecture is built upon the principle of clear modular functional decoupling among distinct subsystems: data acquisition, central processing, display, and power management, thereby optimizing operational stability and minimizing crosstalk between blocks. The voltage from the Li-ion battery is distributed via a charge management circuit and step-down regulators to match nominal voltage levels required by the microcontroller and peripheral components; herein, maintaining low ripple and high stability of the power supply rails is a critical criterion to attenuate power supply noise impacting the highly sensitive, low-amplitude PPG signals. Within this hierarchical configuration, the ESP32-S3 functions as an edge node in an edge computing framework, concurrently executing sensor data ingestion and local preprocessing algorithms prior to coordinating local visualization and upstream transmission to the central server. Consequently, the proposed hardware architecture simultaneously satisfies technical constraints concerning a compact form factor, continuous monitoring capabilities, intuitive display, and strict real-time requirements for a medical wearable device within a centralized healthcare monitoring ecosystem.

3.2. Optical Biosensing Subsystem

Fig. 5 and Fig.6 present the schematic diagrams of the MAX30102 and RTC DS3231, respectively. The optical biosensing subsystem within the system is responsible for acquiring PPG signals to facilitate heart rate computation and SpO_2 estimation. The integrated MAX30102 sensor is utilized to satisfy the form-factor minimization requirement of the wearable device by embedding light-emitting diodes (Red/IR LEDs), a photodiode, and an analog-to-digital converter (ADC)

onto a single chip. Data from the sensor is transmitted to the ESP32-S3 microcontroller via the I²C interface, complemented by the hardware interrupt signal SENSOR_INT to support an event-driven data readout mechanism. To enhance the stability and quality of the acquired signals, the power supply circuitry is designed with isolated domains for logic and LED blocks, while incorporating decoupling capacitors at adjacent interface nodes to minimize power rail noise.

To facilitate continuous monitoring and historical logging, the physiological data samples must be synchronized with accurate real-time reference. Therefore, the RTC subsystem utilizes a specialized DS3231MZ-TR integrated circuit to provide precise timestamps for the entire execution process. The device interfaces with the ESP32-S3 microcontroller via the I²C protocol, minimizing peripheral routing traces and streamlining synchronization with the biosensing module. The circuit operates on a **3.3 V** supply voltage, coupled with a backup battery at the VBAT pin to preserve timekeeping data during primary power outages. Furthermore, the RTC_INT signal line is configured to handle periodic measurement duty-cycling or system wake-up routines. As a result, the acquired heart rate and SpO_2 parameters are managed under a unified chronological framework, satisfying the technical benchmarks of the centralized monitoring architecture.

3.3. Central Control and Processing Subsystem

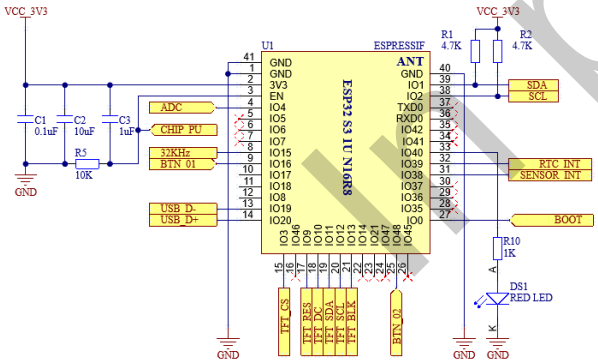

Fig. 7. Schematic diagram of ESP32-S3 core

As illustrated in Fig. 7, the system utilizes an integrated ESP32-S3 microcontroller as its central processing core, leveraging the dual advantages of embedded processing and wide-area wireless communication. Featuring a dual-core Xtensa 32-bit LX7 architecture operating at a clock frequency of **240 MHz**, the microcontroller satisfies all real-time execution constraints, spanning data acquisition, PPG digital filtering, heart rate and SpO_2 algorithm computation, and peripheral display control. Native support for **2.4 GHz** Wi-Fi and BLE facilitates hardware design minimization, effectively conserving PCB real estate for resource-constrained wearable applications. Interfacing between the ESP32-S3 and peripheral functional nodes - specifically the MAX30102 sensor and the DS3231 RTC is established via an I²C bus topology. To guarantee logic-state stability during high-speed communication, the SDA and SCL signal lines are tied to the **3.3 V** power rail through **4.7 kΩ** hardware pull-up resistors.

In addition to its central processing role, the ESP32-S3 coordinates and manages communication with the peripheral subsystems within the system. The hardware interrupt signals, RTC_INT and SENSOR_INT, are routed to dedicated general-purpose input/output (GPIO) pins. This mechanism enables the microcontroller to respond instantaneously via an interrupt-driven architecture, thereby minimizing the computational overhead associated with loop polling routines and optimizing power consumption efficiency. The TFT display interface is connected through a dedicated control signal routing path, supporting the real-time visualization of measured parameters and operational states.

Regarding the hardware auxiliary circuitry, the system integrates a hierarchical decoupling network consisting of 0.1 µF, 1 µF, and 10 µF capacitors in parallel on the 3.3 V power rail to suppress high-frequency noise and stabilize the supply voltage delivered to the microchip. The enable control pin (EN/CHIP_PU) is configured to the appropriate logic level via an external RC circuit to guarantee a reliable power-on reset and boot sequence. Simultaneously, the USB_D+/USB_D- differential signal pair is utilized for program flashing and debugging communication, while the mode configuration pin (BOOT) is designed with external contact pads to facilitate system configuration and firmware deployment. Within this integrated architecture, the ESP32-S3 functions as a comprehensive edge node in the system topology, concurrently executing data acquisition, edge preprocessing, local visualization, and data telemetry to the centralized monitoring platform.

3.4. Power Management Subsystem

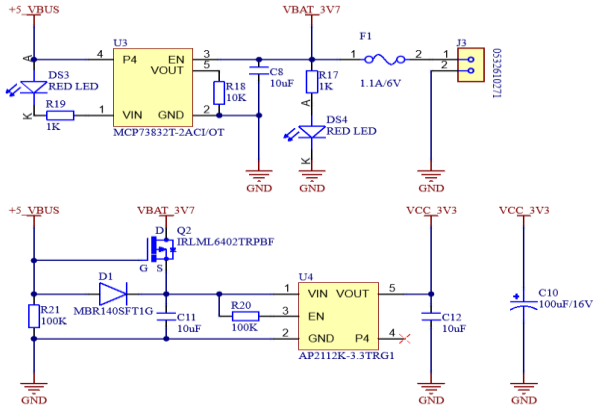

Fig. 8. Schematic diagram of the power supply and battery block for the entire system

The power management subsystem is designed in strict compliance with voltage stability and thermal safety

standards during the charging process, while being optimized for the low-profile geometric constraints of the wrist-worn device. As illustrated in the circuit schematic in Fig. 8, the primary power source of the system utilizes a Lithium-ion (Li-ion) battery with a nominal voltage of **3.7 V**, ensuring the operational autonomy of the device. The charging process is governed by a dedicated MCP73832T integrated circuit - a linear charge management controller designed for single-cell Li-ion batteries. This IC was selected due to its minimal requirement for external auxiliary components, ultra-compact packaging, and optimal efficiency tailored for low-power embedded systems. The integrated MCP73832T solution executes a standard constant current/constant voltage (CC/CV) charging profile aligned with the electrochemical cycle of the battery, while leveraging the status output to drive an LED network for visual indication of the charging phases and cycle termination. To enhance the physical-layer protection mechanism, a polymeric positive temperature coefficient (PTC) resettable fuse is deployed at the power input rail, establishing a proactive solution against overcurrent or short-circuit faults to guarantee system operational safety. Following the power management subsystem, the supply voltage is stepped down and stabilized to a nominal level of **3.3 V** via an AP2112K-3.3 low-dropout (LDO) regulator to power the ESP32-S3 SoC, the sensor subsystem, and other peripheral integrated circuits in the system. This LDO IC was selected for its ultra-low voltage noise density, high output voltage stability, and optimized transient response for noise-sensitive loads, particularly the secondary PPG signal acquisition circuitry. Compared to DC-DC switching regulators, which typically generate substantial ripple noise due to their switching frequencies, utilizing an LDO architecture in this design minimizes conducted power supply noise emissions propagating to the optical biosensing subsystem, thereby significantly enhancing the signal-to-noise ratio (SNR) of the measurement data. Thanks to this optimized Power Distribution Network (PDN) architecture, the system not only satisfies the boundary conditions for the continuous operation of the medical wearable device but also establishes a precise voltage baseline for the central processing, biometric measurement, and wireless communication subsystems to operate reliably across the centralized health monitoring network.

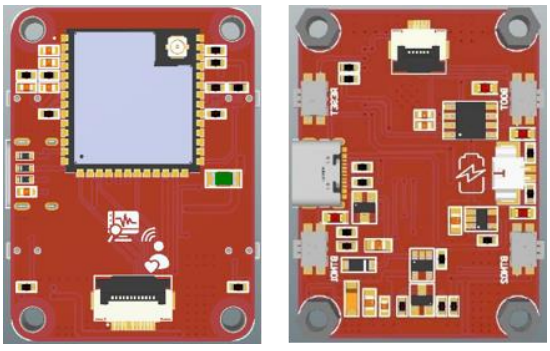

Fig. 9. 3D render of the finalized wearable device

3.5. Printed Circuit Board (PCB)

The 3D render of the finalized device is presented in Fig. 9. The printed circuit board (PCB) layout plays a decisive role in preserving biomedical signal integrity (SI) and optimizing the form factor of the wrist-worn device. The board architecture is implemented on a 2-layer PCB platform applying a strict spatial partitioning strategy between the high-speed digital domain and the sensitive analog domain of the PPG sensor subsystem. To minimize electromagnetic interference (EMI) adversely impacting the optical measurement channel of the MAX30102 IC, the I^2C communication traces are configured using ground shielding techniques and are physically routed away from the radiation zone of the Wi-Fi antenna on the ESP32-S3 SoC. Concurrently, decoupling capacitors are placed with minimal geometric clearance to the V_{cc} power supply pins of the microcontroller and sensor to minimize parasitic loop inductance, thereby effectively suppressing high-frequency noise induced by logic switching processes. The utilization of surface-mount technology (SMT) with standard 0603 and 0402 passive components maximize integration density; as a result, the mainboard is optimally shaped into a rectangular geometry with a size of **40 x 30 mm**, satisfying the stringent mechanical standards of contemporary smartwatch systems.

4. Results and Discussion

4.1. Experimental Prototype and Physical Realization

Fig. 10. The physically realized smartwatch prototype for heart rate and SpO_2 monitoring

Fig. 10 illustrates the physically realized smartwatch engineered by the research team. Leveraging the proposed design strategies, the system hardware was prototyped and fully assembled into a commercial-grade wearable form factor. The empirical results demonstrate that the core integrated circuits, including the ESP32-S3 SoC, the MAX30102 optical biosensor, and the ST7789 TFT display module, are optimally positioned to satisfy the strict spatial constraints dictated by smartwatch architecture. The execution of a 2-layer printed circuit board (PCB) optimizes trace routing while effectively

mitigating electromagnetic interference (EMI) between distinct functional blocks. Furthermore, the protective enclosure was precisely designed and fabricated to maintain a stable, continuous contact pressure between the sensor interface and the subject's skin. This structural solution not only safeguards the signal integrity of the acquired waveforms but also enhances ergonomics for comfortable, long-term operational wear.

4.2. Accuracy Assessment of Vital Signs Indicators

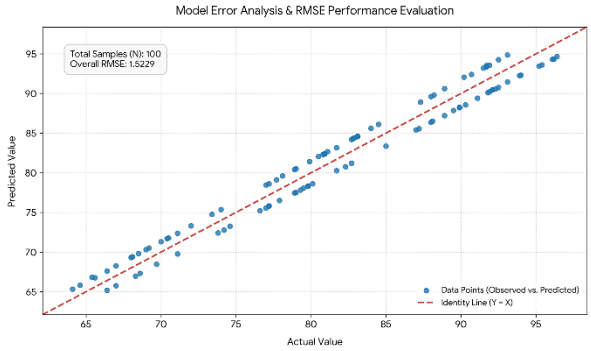

Fig. 11. Heart rate measurement results via the linear correlation plot (RMSE)

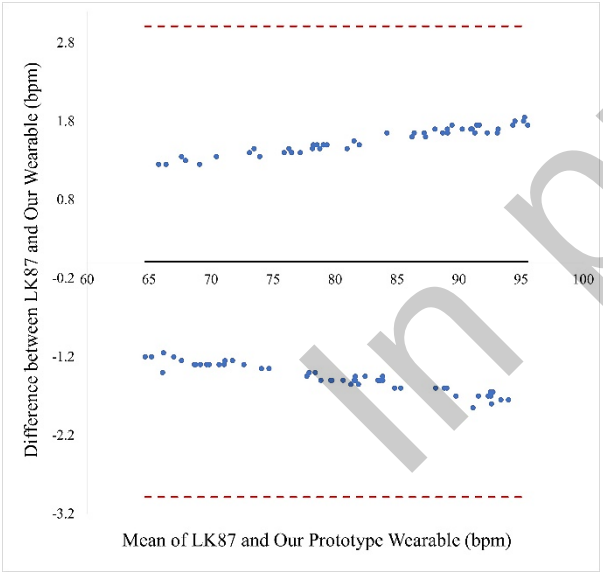

Fig. 12. Heart rate measurement results via the Bland-Altman agreement plot

An experimental prototype was designed to monitor the heart rate and blood oxygen saturation (SpO_2) of elderly inpatients during nocturnal sleep. Nursing staff stationed at a centralized monitoring room inspect a large display at 15-minute intervals to detect any physiological abnormalities. The system features a dual-mode parallel operation mechanism. In the periodic monitoring mode, historical trend data are transmitted to the server at 15-minute intervals for long-term storage and AI-driven analysis. Concurrently, an event-triggered real-time streaming mode is instantly activated whenever heart rate or SpO_2 metrics violate predefined clinical safety thresholds.

Therefore, the LK87 specialized fingertip pulse oximeter was selected as the gold standard reference device. The LK87 is a clinically validated medical device for point-of-care monitoring, operating on the principle of transmissive photoplethysmography (transmissive PPG). The quantitative technical specifications of this reference device include a SpO_2 measurement range of 70% to 99% with an absolute error of ±2%, and a heart rate measurement range of 30 to 240 bpm with an accuracy of ±1 bpm. Establishing the LK87 as a baseline reference enables direct comparative analysis and the quantification of statistical error metrics, thereby visually demonstrating the execution performance of the proposed edge-based signal preprocessing and extraction algorithms on the IoT wearable device.

Preliminary evaluation was conducted on a sample cohort of 100 volunteers across mixed genders, with ages ranging from 50 to 80 years. These volunteers were fully informed regarding biomedical research ethics. Furthermore, the experiments conducted on the samples were intended solely to validate the accuracy of the experimental prototype prior to its clinical implementation on actual patients under the authorization of the medical institution. The experiments were executed under two distinct operational scenarios: a sedentary resting state and light physical activity. For each subject, biometric data acquisition was maintained continuously for a duration of 10 to 15 minutes at a constant sampling frequency of 100 Hz. Throughout the measurement cycle, the volunteers were instructed to minimize high-amplitude mechanical movements of the wrist. This restriction aimed to mitigate the occurrence of motion artifacts that could degrade the signal structure of the reflective PPG waveforms captured by the wearable device.

Fig. 11 and Fig. 12 present the heart rate measurement results via the linear correlation and Bland-Altman agreement plots, respectively. The linear correlation analysis (Fig. 11) illustrates the relationship between the ground-truth values from the LK87 reference device and the predicted values from the experimental prototype across 100 samples. The data points are tightly clustered along the identity line (Y = X), spanning a physiological heart rate range from 65 to 95 bpm. This validates the high accuracy of the prototype wearable device within the standard physiological spectrum. Moreover, the overall root-mean-square error (RMSE) is 1.5229 bpm, which is strictly below the 2-bpm threshold tolerated in wearable medical device literature, further consolidating the reliability of the proposed system for real-time health monitoring applications. To evaluate the systematic bias and limits of agreement (LoA) between the two measurement methods, a Bland-Altman plot (Fig. 12) was constructed. The horizontal axis represents the Mean of the values obtained from both devices, whereas the vertical axis denotes the Difference between the

measurements of the LK87 reference device and the experimental prototype. The mean bias line (solid black line) is positioned very close to the zero baseline, indicating the absence of significant systematic error. The upper and lower LoA bounds (red dashed lines) are established at approximately +3.0 bpm and -3.0 bpm, corresponding to the 95% confidence interval ($Bias \pm 1.96 \times SD$). All 100 data points fall entirely within these boundaries, with no outliers observed outside the region of agreement.

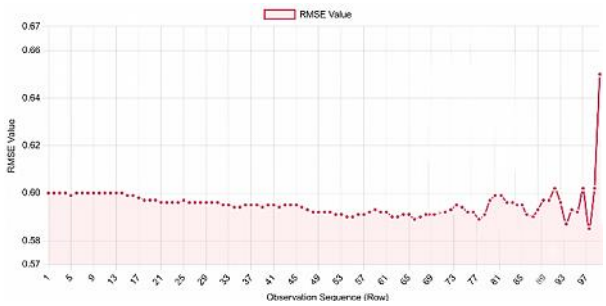

Fig. 13. SpO_2 measurement results via the linear correlation plot (RMSE)

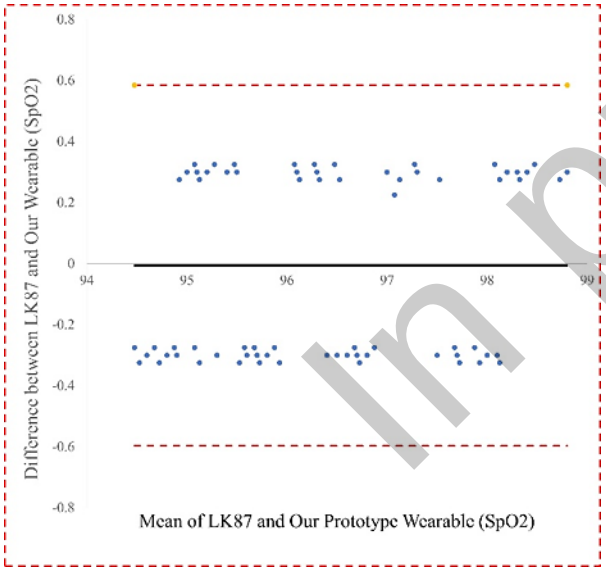

Fig. 14. SpO_2 measurement results via the Bland-Altman agreement plot

Fig. 13 and Fig. 14 present the SpO2 measurement results via the RMSE and Bland-Altman agreement plots, respectively. As shown in Fig. 13, the overall RMSE fluctuates within an extremely narrow margin, ranging from 0.585% to 0.65% with the permissible error tolerance for commercial medical devices is ≤ 2%. Therefore, the error margin of below 0.66% exhibited by the experimental prototype demonstrates superior accuracy. Furthermore, from samples 1 to 75, the RMSE maintains high linear stability, hovering around 0.59% to 0.60%. In the latter phase of the sequence (from samples 76 to 100), the plot exhibits minor sinusoidal oscillations, reaching a transient peak of 0.65% at sample 100. This phenomenon typically reflects the presence of mild motion artifacts induced by postural adjustments of the volunteers or optical degradation (PPG signal attenuation) during the concluding stage of the prolonged testing session.

The Bland-Altman plot (Fig. 14) was constructed to provide an in-depth analysis of the error characteristics between the two devices within the physiological range of 94.5% to 99%. The mean bias line (solid black line) coincides perfectly with the zero baseline (0% bias). This demonstrates that the calibration algorithm of the wearable device achieves an ideal equilibrium, exhibiting no systematic tendency toward either overestimation or underestimation relative to the LK87 reference device. The upper and lower limits of agreement (LoA) are strictly defined at +0.58% and -0.60%, respectively (indicated by the red dashed lines). The entire experimental dataset (100%) is tightly clustered within this LoA interval, with absolutely no clinical outliers detected.

4.3. Power Consumption Performance and Power Management

Table 1 presents the estimated power consumption of the device across various operational modes. The power consumption profile is a critical technical metric that dictates the operational lifetime and mobility of a smart wearable system intended for continuous medical monitoring. Quantitative experimental evaluation of the core hardware components established a detailed power distribution profile under specific operational modes; these results provide a scientific baseline to experimentally validate the feasibility, reliability, and operating efficiency of the proposed power management unit (PMU).

The ESP32-S3 system-on-chip (SoC) - acting as the central microcontroller unit (MCU) of the system - consumes a nominal average current of 65 mA during the execution of edge computing and signal preprocessing tasks. However, during medical telemetry data transmission cycles to the cloud server via the MQTT protocol, the recorded peak current reaches a maximum of 240 mA, which is an inherent consequence of the activation and high-power operation of the integrated on-chip Wi-Fi radio frequency (RF) transceiver. Regarding the display subsystem, the TFT display driven by the dedicated ST7789 IC requires a maximum current consumption of approximately 45 mA when operating at peak backlight brightness, thereby ensuring an adequate contrast ratio and visual readability under complex ambient light conditions. Conversely, the MAX30102 optical sensor integrated circuit operates in an ultra-low-power mode, maintaining a working current of only approximately 1.2 mA during continuous data acquisition cycles, which significantly mitigates load stress on the power distribution network and optimizes the overall power budget of the wearable system.

Table 1. Power consumption estimation results of the device across various operational modes

Operation mode	Primary Active Components	Average Current Consumption (mA)	Peak Current (mA)	Approximate Power Dissipation at 3.7 V (mW)
Deep Sleep	RTC timekeeping; ESP32-S3 in deep-sleep state	0.01	0.05	0.04
Standby	ESP32-S3 idle; active RTC; TFT display OFF; sensors in standby	18	25	66.6
Local Measurement (Display OFF)	ESP32-S3 processing PPG; MAX30102 continuous sampling; active RTC	65	85	251.6
Local Measurement & Display	ESP32-S3; MAX30102; TFT display (medium brightness); active RTC	92	120	340.4
Periodic MQTT Transmission (15 minutes/time)	ESP32-S3 processing; duty-cycled Wi-Fi transmission (15-min interval); MAX30102; TFT; RTC	45	240	155
Maximum / Peak Load	Continuous Wi-Fi activity; TFT display (maximum brightness); continuous sampling	128	245	473.6
Battery Charging (Load Disconnected)	MCP73832T charging controller	300 – 500	500	1500-2500

To maximize battery runtime during prolonged medical monitoring scenarios, the system is configured to dynamically transition into Deep Sleep mode during idle states of the data acquisition process. In this mode, most internal functional subsystems and the central MCU are power-gated, reducing the quiescent current to a minimum of approximately 10 µA. Simultaneously, the battery charge management subsystem exhibits stable performance through dynamic current regulation within a range of 100 mA to 500 mA, ensuring a safe energy replenishment cycle and optimizing charging duration via a standard physical-layer interface. These quantitative experimental parameters robustly validate the device's capability to fully satisfy continuous uptime constraints in long-term clinical applications, while establishing a solid technical foundation for the reliability and availability of a dedicated IoT network node within healthcare environments.

4.4. Communication Evaluation and Centralized Monitoring Capability

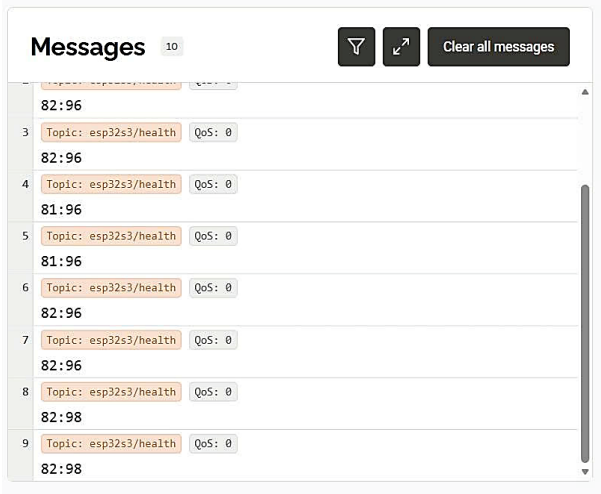

Fig. 15. MQTT interface

In order to satisfy the constraints of centralized multi-patient real-time monitoring with minimal latency and optimized bandwidth usage, the system implements the Message Queuing Telemetry Transport (MQTT) protocol for wireless telemetry. Following data acquisition, decoding, and parameter extraction (BPM and SpO2) by the ESP32-S3 microcontroller, the computed metrics are encapsulated with a standardized real-time timestamp and a unique Device ID into a compact JSON format. The edge device, acting as an MQTT Client, establishes a wireless link via 2.4 GHz Wi-Fi to publish the data packets to an MQTT Broker (such as HiveMQ or Mosquitto) at a predetermined periodic interval (e.g., every 2 seconds as a real mode). Dedicated communication topics enable the central server to subscribe and parse incoming payloads accurately, effectively mitigating data collision and stream conflicts during network scaling.

The data transmission performance via the MQTT protocol is quantified based on two core metrics: network latency and data integrity at the centralized server. The device network node encapsulates medical biometric parameters into a JSON payload structure and executes the publishing process to specific designated topics at a fixed periodic interval of 15 minutes as a periodic monitoring mode (in Fig. 15). Experimental results demonstrate that the centralized monitoring architecture is capable of concurrent multi-node data acquisition without incurring network congestion or packet loss. The end-to-end latency–measured from the instance of signal acquisition by the sensor subsystem to the visual data update on the centralized dashboard–achieves an optimal level, strictly satisfying the real-time constraints required for emergency clinical alert triggering mechanisms. This centralized structured management capability enables healthcare personnel to simultaneously monitor the physiological state variations of multiple patients with high clarity and precision.

Table 2. Comparative summary with existing related work

Study	Microcontroller Platform	Communication Protocol	Signal Processing Algorithm (PPG)	Monitoring Capability	Key Research Limitations
Xie et al. [1] (2025)	STM32 / ARM Cortex	Bluetooth Low Energy (BLE)	Basic time-domain analysis	Individual (Smartphone-dependent)	Restricted transmission range (<10); lacks centralized multi-device management.
Ghadi et al. [12] (2025)	Raspberry Pi Zero	Wi-Fi / HTTP	Cloud-based AI processing	Local / Centralized	Bulky form factor; high power consumption; severe latency in cloud feedback loops.
Sharma et al. [13] (2024)	Arduino Nano 33 BLE	Wi-Fi / CoAP	Low-pass filtering	Centralized (Small-scale)	Lacks local edge display interface; limited hardware resources for multi-tasking expansion.
Proposed Work (This Study)	ESP32-S3	Wi-Fi / MQTT (Independent Broker)	Kalman / Edge AI	Centralized (Multi-device / Cloud)	Lacks dedicated hardware thermal dissipation; advanced medical-grade encryption standards are yet to be integrated.

4.5. Comparative Analysis with Related Works

To underscore the efficacy and contributions of the proposed system, a comprehensive comparative analysis was performed against recent related works published during the 2024–2025 period. The detailed benchmarking results - encompassing hardware platforms, communication protocols, PPG signal processing algorithms, monitoring capabilities, and technical limitations - are consolidated in Tab. 2.

4.5.1. Hardware platform and communication protocol analysis

Regarding hardware architecture and connectivity, the proposed system utilizes an ESP32-S3 microcontroller integrated with the Wi-Fi/MQTT protocol via an independent broker. This approach successfully overcomes the constraints of a limited transmission range (less than 10 m) and the multi-device management deficiencies inherent in the STM32 and Bluetooth Low Energy (BLE) configuration presented by Xie *et al.* [1]. Although the solution by Ghadi *et al.* [11] leveraging a Raspberry Pi Zero offers high computational performance, this configuration suffers from major drawbacks regarding its bulky physical form factor and high-power consumption, rendering it unsuitable for mobile medical wearables. Conversely, the integration of the ESP32-S3 chip in this study ensures an optimal trade-off among processing capability, physical dimensions, and power efficiency, outperforming *resource-constrained hardware solutions* such as the Arduino Nano 33 BLE adopted by Sharma *et al.* [12].

4.5.2. Signal processing algorithms and computing architecture

The core technical distinction of this study lies in the localized deployment of an adaptive Kalman filtering algorithm coupled with Edge Artificial Intelligence (Edge AI) executed directly on device. While conventional remote health monitoring frameworks rely heavily on cloud-based processing–thereby suffering from severe feedback latency and intensive network bandwidth utilization–the proposed architecture leverages the native dual-core computational capability of the ESP32-S3 microcontroller to establish a robust **Edge Intelligence** layer. This paradigm completely resolves the high response latency and communication bottlenecks inherent in the cloud-centric AI architecture proposed by Ghadi *et al.* [12]. Instead of transmitting raw, noise-corrupted data telemetry streams, the on-chip implementation of the Adaptive Edge-based Kalman Filter (AE-KF) serves as an intelligent data preprocessor. Specifically, by dynamically modulating the process and measurement noise covariance matrices (Q_k and R_k) via a localized directional derivative operator, the edge node independently mitigates wrist-specific motion artifacts while preserving the underlying physiological morphology of the PPG waveforms.

Consequently, our edge-centric filtering and analysis methodology yields superior accuracy in PPG signal denoising compared to the conventional low-pass filters utilized by Sharma *et al.* [13] or the basic time-domain analysis solutions developed by Xie *et al.* [1]. Edge-centric processing not only minimizes network transmission throughput but also guarantees real-time responsiveness critical for emergency medical alert applications. Ultimately, the AE-KF framework does not merely filter transient signal ripples; it establishes a standardized, high-SNR data infrastructure that directly optimizes the system for seamless downstream integration with deep learning prognostic models.

4.5.3. Centralized monitoring and scalability analysis

In terms of operational capacity, the proposed system demonstrates a robust cloud-integrated, centralized multi-device monitoring capability, offering significantly superior scalability compared to the smartphone-dependent personal monitoring model of Xie *et al*. [1] or the small-scale topologies of Sharma *et al.* [13]. The deployment of an independent

MQTT broker enables the system to concurrently manage high-throughput data streams from multiple patients simultaneously without incurring network congestion.

5. Conclusions

This study has comprehensively achieved the architectural design and experimental prototyping objectives of an IoT-integrated wearable medical device, effectively facilitating the continuous monitoring of heart rate and blood oxygen saturation (SpO_2) within a centralized patient monitoring framework. By leveraging the hardware infrastructure of the ESP32-S3 system-on-chip (SoC) in synchronous integration with the dedicated MAX30102 optical sensor IC, the system has experimentally validated high-accuracy biomedical digital signal processing capabilities at the edge. The experimental prototype demonstrates high accuracy and strong agreement with the LK87 reference device RMSE = 1.5229 bpm, with a maximum error within ± 3 bpm). Furthermore, blood oxygen saturation (SpO_2) evaluation yields exceptional compatibility and precision, characterized by a peak RMSE of less than 0.65% and an ultra-narrow Bland-Altman limit of agreement (LoA) interval of [+0.58%, -0.60%].

Although the prototype demonstrates feasible performance under standard static measurement configurations, the reflective PPG signal structure captured at the wrist biometric site exhibits high susceptibility to motion artifacts (MAs) when subjects operate under high-intensity dynamic scenarios. Furthermore, the current system validation is restricted to preliminary field testing on a cohort of healthy individuals and has not yet undergone rigorous clinical validation within specialized healthcare facilities to comprehensively assess its performance against actual pathological manifestations.

In particular, the future research roadmap is deeply oriented toward integrating advanced machine learning and deep learning models to uncover structural features and perform in-depth analysis of the acquired physiological time-series data. The deployment of these classification algorithms and predictive modeling paradigms enables the establishment of early detection and prognostic warning mechanisms for critical cardiovascular and respiratory pathological syndromes, specifically arrhythmia or acute respiratory failure complications. Consequently, this solution fundamentally shifts the operational paradigm of the system from a passive reactive monitoring state to an architecture capable of providing proactive clinical diagnostic support and remote preventive healthcare.

Future iterations of the prototype will focus on optimizing the physical layout to resolve localized hardware heat dissipation issues during continuous operation. Additionally, to transition this edge-computing architecture into commercial telehealth ecosystems, future research will integrate advanced medical-grade security encryption standards (such as AES-GCM or lightweight hardware-accelerated cryptographic primitives) directly onto the ESP32-S3 platform to ensure strict patient data privacy.

References

[1] H. Xie, L. Yang, B. Jiang, Z. Huang, and Y. Lin, State-of-the-art wearable sensors for cardiovascular health: a review, npj Cardiovascular Health, vol. 2, Oct. 2025, Art. no. 53. https://doi.org/10.1038/s44325-025-00090-6

[2] R. Uddin and I. Koo, Real-time remote patient monitoring: A review of biosensors integrated with multi-hop IoT systems via cloud connectivity, Applied Sciences, vol. 14, is. 5, Feb. 2024, Art. no. 1876. https://doi.org/10.3390/app14051876

[3] J. Allen, Photoplethysmography and its application in clinical physiological measurement, Physiological Measurement, vol. 28, no. 3, pp. R1–R39, Feb. 2007. https://doi.org/10.1088/0967-3334/28/3/R01

[4] K. B. Kim and H. J. Baek, Photoplethysmography in wearable devices: a comprehensive review of technological advances, current challenges, and future directions, Electronics, vol. 12, iss. 13, Jul. 2023, Art. No. 2923. https://doi.org/10.3390/electronics12132923

[5] D. Lapsa, R. Janeliukstis, M. Metshein, and L. Selavo, PPG and bioimpedance-based wearable applications in heart rate monitoring—a comprehensive review, Applied Sciences, vol. 14, iss. 17, Aug. 2024, Art. 7451. https://doi.org/10.3390/app14177451

[6] W.-K. Beh, Y.-C. Yang, and A.-Y. Wu, Quality-aware signal processing mechanism of PPG signal for long-term heart rate monitoring, Sensors, vol. 24, iss. 12, Jun. 2024, Art. no. 3901. https://doi.org/10.3390/s24123901

[7] P. H. Charlton, V. Marozas, E. Mejía-Mejía, P. A. Kyriacou, and J. Mant, Determinants of photoplethysmography signal quality at the wrist, PLOS Digital Health, vol. 4, iss. 6, Jun. 2025, Art. no. e0000585. https://doi.org/10.1371/journal.pdig.0000585

[8] R. Kirszenblat and P. Edouard, Validation of the withings scanwatch as a wrist-worn reflective pulse oximeter: prospective interventional clinical study, Journal of Medical Internet Research, vol. 23, no. 4, Apr. 2021, Art. no. e27503. https://doi.org/10.2196/27503

[9] K. D. Torp, P. Modi, E. J. Pollard, and L. V. Simon, Pulse oximetry, in StatPearls [Internet], Treasure Island (FL): StatPearls Publishing, updated Jul. 30, 2023.

[10] N. Fong, M. S. Lipnick, E. Behnke, Y. Chou, S. Elmankabadi, L. Ortiz, C. S. Almond, I. Auchus, G. W. Burnett, R. Bisegerwa, D. R. Conrad, C. M. Hendrickson, S. Hooli, R. Kopotic, G. Leeb, D. Martin, E. D. McCollum, E. P. Monk, K. L. Moore, L. Shmuylovich, J. B. Scott, A.-K. I. Wong, T. Zhou, R. Pirracchio, P. E. Bickler, J. Feiner, and T. J. Law, Open access dataset and common data model for pulse oximeter performance data, Scientific Data, vol. 12, Apr. 2025, Art. no. 570.

https://doi.org/10.1038/s41597-025-04870-8

[11] M. Cao, R. Ramezani, V. K. Katakwar, W. Zhang, D. Boda, M. Wani, and A. Naeim, Developing remote patient monitoring infrastructure using commercially available cloud platforms, Frontiers in Digital Health, vol. 6, Nov. 2024, Art. no. 1399461. https://doi.org/10.3389/fdgth.2024.1399461

[12] D. Silva, L. I. Carvalho, J. Soares, and R. C. Sofia, A performance analysis of Internet of things networking protocols: Evaluating MQTT, CoAP, OPC UA. Applied Sciences, vol. 11, iss. 11, may. 2021, Art. no. 4879. https://doi.org/10.3390/app11114879